Applied Catalysis B: Environmental 92 (2009) 209–216

Contents lists available at ScienceDirect

Applied Catalysis B: Environmental

journal homepage: www.elsevier.com/locate/apcatb

Non-precious oxygen reduction catalysts prepared by high-pressure pyrolysis for low-temperature fuel cells

R. Kothandaraman [a,1], Vijayadurga Nallathambi [a], Kateryna Artyushkova [b], Scott Calabrese Barton [a,*]

[a] Department of Chemical Engineering and Materials Science, Michigan State University, East Lansing, MI 48824, USA
[b] Department of Chemical and Nuclear Engineering, University of New Mexico, Albuquerque, NM 87131, USA

ARTICLE INFO

Article history:
Received 19 December 2008
Received in revised form 29 June 2009
Accepted 9 July 2009
Available online 17 July 2009

Keywords:
Electrocatalysis
Oxygen reduction reaction
Non-precious catalysts
Pyrolysis
XPS
Fuel cells

ABSTRACT

Iron-based catalysts for the oxygen reduction reaction (ORR) were produced by pyrolysis of iron-acetate and Ketjenblack® carbon with varying amounts of 2,2′-bipyridine in a closed, constant-volume vessel. The total surface nitrogen content detected by XPS varied from 0.6 to 2.2 at% when the nitrogen precursor loading was varied from 1.5 to 11.3 wt%. The amount of nitrogen in the Fe-pyridinic form is estimated to vary between 0.12 and 0.24 at%, correlating to catalytic activity (current density) variation from 0.07 to 1.9 mA cm^{-2} at a catalyst loading of 0.5 mg cm^{-2}. These results support the theory that iron associated with pyridinic nitrogen is a component of the catalytic active site responsible for oxygen reduction.

1. Introduction

The increasing cost of precious metals has accelerated efforts to replace Pt-group metals with cost-effective non-precious metal catalysts for the oxygen reduction reaction (ORR) in low-temperature fuel cells, such as Polymer Electrolyte Fuel Cells (PEFCs) and Direct Methanol Fuel Cells (DMFCs). Catalysts based on transition metals such as Fe and Co have demonstrated ORR activity, albeit lower than that of platinum [1]. Such catalysts also exhibit selectivity towards ORR in the presence of a methanol, enabling concentrated methanol feed and increased volumetric energy density in DMFCs [2–5].

Jasinski discovered the catalytic nature of cobalt pthalocyanine [6] and subsequently catalysts were produced by pyrolyzing metal-N_4 macrocycles adsorbed on carbon black in inert atmosphere [7]. However, despite being considered non-precious, these metal macrocycles are expensive precursors [5]. Yeager et al. demonstrated that only a metal-nitrogen center is required, not the entire macrocycle, by producing an active catalyst for ORR by pyrolysis of a metal precursor (Cobalt acetate), carbon black and a nitrogen precursor (poly-acrylonitrile) in an inert atmosphere [8]. Following this approach, many methods have been developed to prepare non-precious metal catalysts, such as heat-treating carbon-supported organometallic complexes [9,10], pyrolyzing metal and carbon precursors in ammonia or acetonitrile atmosphere [11–13], co-sputtering Co or Fe and carbon in a dinitrogen atmosphere with or without subsequent heat-treatment [14], and mixing N-containing ligands with a cobalt oxide sol, followed by entrapment in a carbon-supported polypyrrole matrix [15].

The structure of the metal-nitrogen-carbon (MNC) catalytic sites and the mechanism of ORR at these sites remain uncertain. Based on time-of-flight secondary ion mass spectrometry results, Lefevre et al. suggested FeN_4/C or CoN_4/C as the catalytic active sites, in which pyridinic nitrogens are associated with a single spanning metal center [16,17]. Using ammonia gasification of defect sites in metal-loaded pristine carbon, they introduced N-enriched micropores that acted as active centers for ORR. Recently, the same workers pyrolyzed a highly ordered synthetic graphite powder of low surface area (3.5 m^2 g^{-1}) along with an iron precursor (e.g. iron acetate) in an ammonia environment [18]. The catalysts thus produced exhibited an N content as high as 4 at%. As the graphite crystallite size decreased, the degree of disorder, nitrogen content, and microporous (<22 Å) specific surface area increased, as did the catalytic activity.

Ozkan et al. [19,20] and Stevenson et al. [21] identified nitrogen-containing edge planes without metal as active sites. Popov et al. proposed that active sites containing pyridinic nitrogen are responsible for the catalytic activity for ORR and

* Corresponding author. Tel.: +1 517 355 0222.
E-mail address: scb@msu.edu (S.C. Barton).
[1] National Research Council, Ottawa, K1A 0R6 Canada.

0926-3373/$ – see front matter © 2009 Elsevier B.V. All rights reserved.
doi:10.1016/j.apcatb.2009.07.005

reported low-level evolution of H_2O_2, an undesirable intermediate, when reducing oxygen in acidic medium [22]. Ruggeri et al. proposed that surface pyridinic nitrogen in co-ordination with iron forms the catalytically active site [23]. Following this, Charreteur et al. proposed a possible active site, which contains pyridinic N in a phenanthroline environment present at graphitic crystallite edges. N present in two adjacent crystallites than coordinate with Fe to form an active site of the form FeN_{2+2}/C [24]. The presence of MN_4 active sites in catalysts pyrolyzed at temperatures above 800 °C was confirmed by Ziegelbauer et al. using $\Delta\mu$ XANES analysis [25], and such sites were proposed to achieve complete, 4 e^- reduction of oxygen. Recently, Wood et al. [26] produced highly active catalysts that showed a volumetric current density of 19 A cm^{-3} using metal-doped nitroaniline as the nitrogen source. Their catalysts contained nearly the same amount of iron (6 $\mu g\ cm^{-2}$) as Ruggeri et al. but with two-fold higher surface nitrogen content (4%). This was considered as further evidence that iron may not be a part of the catalytic active site [22]. Similarly, Wei et al. reported an increase in catalytic activity of pyrolyzed Co–N/C with increasing surface concentration of nitrogen [27].

Fig. 1 indicates various nitrogen functionalities that may be present in the carbon-support. Most literature studies report two types of catalytic sites: a low-temperature site wherein a metal atom is coordinated with four nitrogen atoms, and a high-temperature site wherein metal atoms coordinate with two nitrogens [17,25,28,29]. Iron oxide has also been proposed as a site of lower activity [12]. Among the surface nitrogen groups, two types of N are widely cited [22,25,30,31]. One is quaternary nitrogen present in the plane of graphene sheets (Fig. 1), often described as graphitic nitrogen, and not catalytically active. The second nitrogen species is pyridinic, wherein nitrogen atoms present at the edge of graphene layers bind to two carbon atoms and retain two-free electrons that can coordinate with metal ions. In the literature, formation of pyridinic $N^+–O^-$ species was observed during exposure to oxygen [30,32,33], which suggests a possible mechanism of oxygen reduction.

In addition to the transition-metal and nitrogen precursors, the carbon-support and the method by which these catalysts are synthesized play a critical role in determining the activity of the catalyst towards ORR. In our approach, a nitrogen source (2,2′-bipyridine), a high surface area carbon source (Ketjenblack® 600JD) and a metal precursor (iron-acetate) were pyrolyzed together in a closed container (quartz ampule), generating autogenic pressure due to bipyridine evaporation and subsequent decomposition. The synthesis was designed to increase the activity of the nitrogen precursor around the carbon-support while maintaining nitrogen mobility, thereby increasing the density of nitrogen-based catalytic sites. As nitrogen is believed to be a component of the catalytic site, increasing the surface nitrogen density could potentially increase active site density. The morphology of the pyrolyzed catalysts was analyzed by nitrogen physisorption, the composition was studied by X-ray photoelectron spectroscopy (XPS) and CHN combustion analysis, and the activity of the catalysts was assessed electrochemically using the thin-film rotating disk and rotating ring-disk electrode techniques. Deconvolution of the XPS spectra allowed correlation of electrochemical activity with the concentration of iron sites associated with pyridinic moieties.

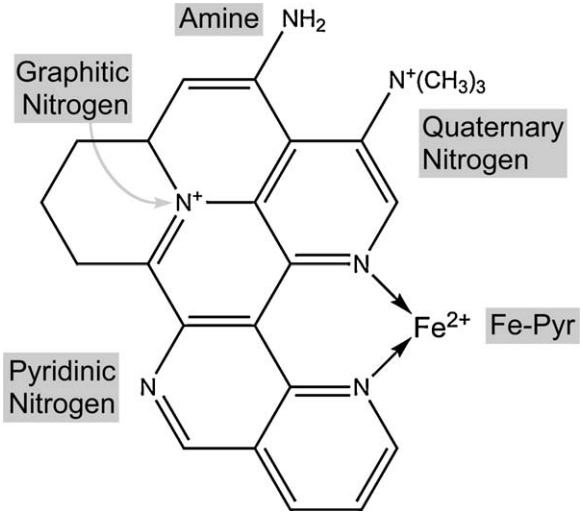

Fig. 1. Nitrogen functional groups present on pyrolyzed metal-nitrogen-carbon catalyst surfaces.

2. Experimental

Iron (II)-acetate, Nafion® solution (1100 EW, 5 wt%) and sulfuric acid (ACS grade) were obtained from Alfa Aesar (Ward Hill, MA). 2-2′-bipyridine was obtained from Fluka (St. Louis, MO). Ketjenblack® 600JD carbon black was obtained from Akzo Nobel (Chicago, IL). Carbon-supported platinum (20 wt% Pt/C) was purchased from BASF Fuel Cell (Somerset, NJ). Potassium ferricyanide, ($K_3Fe(CN)_6$, ACS grade) was obtained from Spectrum Chemical (Gardena, CA), and sodium hydroxide (NaOH, ACS grade) was obtained from J.T. Baker (Phillipsburg, NJ). Pressurized oxygen cylinders were obtained from Airgas (Lansing, MI). All materials were used as received.

2.1. Catalyst synthesis

Ketjenblack® 600JD, used as carbon-support, was dispersed in a 95 wt% ethanol solution, to which iron (II)-acetate corresponding to 1.6 wt% Fe was added. This slurry was stirred for about 6 h followed by solvent evaporation to yield a dry powder. Powder samples of 55 mg were ground with 2,2′-bipyridine in amounts ranging from 5 to 125 mg, and this powder was subsequently charged into a 1.7 mL quartz ampule. The ampule was flame-sealed under vacuum, and subjected to heat-treatment at 700–900 °C in a tube furnace for 5 h. At around 272.5 °C, bipyridine vaporizes, increasing the pressure inside the vessel, and decomposes at elevated temperature, enabling nitrogen fixation within the carbon-support. Assuming the vapor phase inside the ampule to be an ideal gas, vapor pressure at 800 °C due to vaporized bipyridine ranges from 32 to 665 psi while varying nominal N content from 1.5 to 11.3 wt%. When calculating these values, a correction was included for the volume occupied by carbon in the quartz ampoule, as Ketjenblack® carbon has a low bulk density (115 kg m^{-3}).

2.2. Physical and Chemical Characterization

Surface analyses of the catalysts by X-ray photoelectron spectroscopy (XPS) utilized a Kratos Analytical AXIS Ultra DLD Imaging System with an Al K-alpha X-ray source operating at 225 W. The base pressure was 2×10^{-10} torr and the operating pressure was 2×10^{-9} torr. Charge neutralization was used for all samples to prevent charge accumulation. Three 700 $\mu m \times 350\ \mu m$ areas per sample were analyzed. The survey (low-resolution wide scan) was acquired at 80 eV pass energy for 6 min. High-resolution N 1s and C 1s spectra were acquired at 20 eV pass energy for 20 and 8 min respectively.

Data analysis and quantification were performed using CasaXPS software. A linear background subtraction was used for quantification of C 1s, O 1s and N 1s, while a Shirley background was applied to Fe 2p spectra. Sensitivity factors provided by the manufacturer

were utilized. All the spectra were charge-referenced to aromatic carbon at 284.7 eV. A 70% Gaussian/30% Lorentzian line shape was utilized in the curve-fit. Curve-fitting was carried out using individual peaks of constrained width and shape.

Surface nitrogen content of the pyrolyzed samples was also evaluated by CHN (CE440 CHN analyzer, Microanalysis Laboratory, University of Illinois, Urbana, IL) to quantify bulk amounts of C, H and N. Surface area and pore size analysis were performed using nitrogen adsorption in a Micromeritics Gemini V BET analyzer that implements the Barrett–Joyner–Halenda (BJH) method [34].

2.3. Electrochemical characterization

Electrochemical characterization was conducted using a glassy carbon rotating disk electrode (RDE, 0.2 cm^2 area) and a rotating ring-disk electrode (RRDE, Pine Research Instrumentation, Raleigh, NC) having a glassy carbon disk (0.25 cm^2 disk area) and a platinum ring (6.25 mm inner diameter, 7.92 outer diameter). All experiments were conducted in aqueous 1N sulfuric acid at 40 °C. Potential was measured relative to an $Hg|Hg_2SO_4$ reference electrode (0.68 V/SHE) and all potentials were corrected to the SHE scale. A platinum wire served as the counter electrode. The catalyst ink was prepared by dispersing 4 mg of the catalyst powder ultrasonically in a solution mixture containing 150 μL isopropyl alcohol and 50 μL Nafion® (5 wt% solution). A catalyst loading of 0.5 mg cm^{-2} was achieved by depositing appropriate amount of the suspension on the glassy carbon electrode followed by drying for 10 min at 60 °C. The electrode thus obtained was immersed in a solution of 1N H_2SO_4 saturated with O_2. Linear-sweep voltammograms were recorded in the potential range 0.85–0.2 V/SHE at a scan rate of 0.5 mV s^{-1} and 1200 rpm rotation rate.

The collection efficiency, $N = I_{ring}/I_{disk}$, for the RRDE was verified using the disk electrode loaded with carbon-supported platinum at 14 μg_{Pt} cm^{-2}, which catalyzed the reduction of ferricyanide from 10 mM $K_3[Fe(CN)_6]$ in deaerated aqueous 0.1 M NaOH, followed by re-oxidation at the ring electrode poised at 1.5 V/RHE [35]. A collection efficiency $N = 0.39 \pm 0.01$ was observed, independent of disk potential and rotation rate, and consistent with manufacturer specifications. The fraction of H_2O_2 generated during oxygen reduction was measured with the platinum ring poised at 1.2 V while the potential of the disk electrode was scanned.

3. Results and discussion

Oxygen reduction catalysts were prepared from iron-acetate, bipyridine, and Ketjenblack® precursor materials with varying bipyridine proportions such that nominal nitrogen content varied from 0 to 11.3 wt%. Fig. 2a shows the differential surface area, determined by BJH analysis of nitrogen desorption, of Ketjenblack® 600JD and catalysts of selected nitrogen content. Most of the observed pore area occurs at pore sizes ranging between 20 and 60 Å. A peak in pore area at 35 Å pore width decreases in amplitude (and slightly in peak pore width) with increasing nitrogen content such that it reaches 64% of its initial value at 10.3 wt% nominal nitrogen. Pore area in the microporous region at 20 Å and below is small, which is expected for Ketjenblack® [12].

The total BET surface area of all catalysts is presented in Fig. 2b. A 51% decrease in BET surface area from 1440 m^2 g^{-1} can be observed when the nominal N content increases from 1.5 to 6.9 wt%, likely due to the pore closure by bipyridine decomposition products within micropores of less than 4 nm diameter. Above 6.9 wt% (nominal) N, the surface area stabilizes in the range of 700–900 m^2 g^{-1}, possibly due to the accumulation of amorphous carbon structures obtained from bipyridine. However beyond 10.9 wt%, there is a large decrease in the surface area, likely due to incomplete decomposition of deposited bipyridine from supersaturated bipyridine vapor, leading

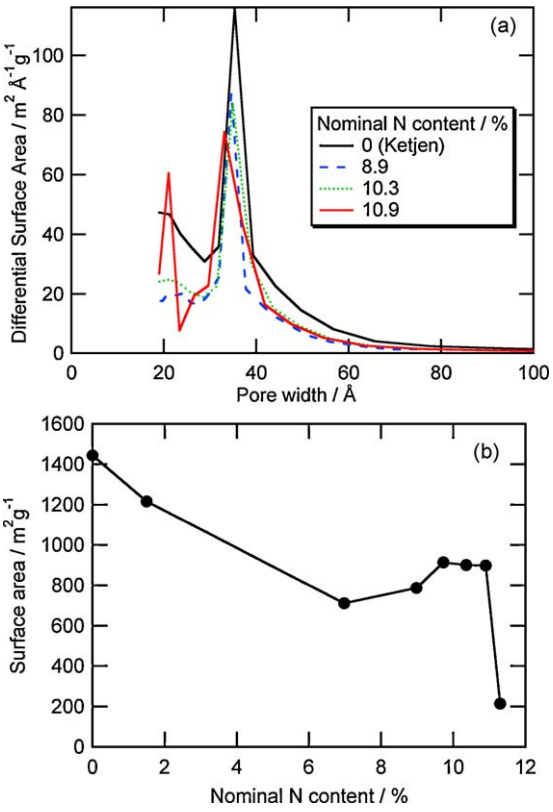

Fig. 2. Effect of nitrogen content on surface morphology. (a) Differential surface area distribution of various catalysts obtained from BJH desorption. (b) Observed BET surface area for various catalysts.

Table 1
Catalyst yield with varying bipyridine content.

Nominal nitrogen content (wt%)	Initial mass[a] (mg)	Product mass[b] (mg)
1.5	60	57.5
6.9	90	69.0
8.9	110	66.5
9.7	120	65.0
10.3	130	66.5
10.9	140	68.0
11.3	160	123.0
12.5	180	138.0

[a] Includes 53 mg Ketjenblack® 1.7 mg Fe-acetate and sufficient bipyridine to achieve the indicated mass.
[b] Mean product mass of two batches.

to increased pore blocking. As evident from Table 1, a large increase in post-pyrolysis mass and a steep decrease in surface area can be observed confirming that the bipyridine is not decomposed completely. Even at 10.9 wt% N, the large increase in surface area at 20 Å pore size (Fig. 2) may be explained by the deposition of amorphous carbon material from bipyridine. Similar partially decomposed organic moieties have been reported in the literature. From the results of Raman spectra, Charreteur et al. [24] proved the presence of amorphous organic molecules in developmental carbon black due to the injection of CH_4 during carbon black production. Pylypenko et al. [36] reported the presence of pyrolysis products comprising carbon, nitrogen and metal atoms with intermediate stoichiometry. Sun et al. [37] found that the surface area of their catalyst decreased linearly with increased loading of iron in the form of an iron porphyrin. They hypothesized that either metal nanoparticles block pores in the support or that metal chelates or fragments chemically bind to the support surface.

Table 2
Elemental quantification by XPS.

Nominal N (wt%)	Pyrolysis Temp. (°C)	C 1s (at%)	O 1s (at%)	N 1s (at%)	Fe 2p (at%)
1.5 (no Fe)	–	98.3	0.7	0.97	–
1.5	–	97.0	2.0	0.37	0.15
1.5	800	97.7	1.8	0.60	0.06
6.9	800	97.0	1.6	1.32	0.11
8.9	800	96.8	1.4	1.68	0.09
9.7	800	97.3	1.4	1.24	0.10
10.3	700	97.4	1.1	1.26	0.27
10.3	800	97.4	1.2	1.14	0.13
10.3	900	98.6	0.6	0.64	0.11
10.9	800	97.3	1.3	1.23	0.16
11.3	800	96.1	1.6	2.18	0.15

High-resolution spectra obtained from X-ray photoelectron spectroscopy (XPS) were processed to obtain elemental quantification. Seven nitrogen compositions were considered, and unpyrolyzed samples of 1.5 wt% N, with and without iron-acetate, were also analyzed. The effect of pyrolysis temperature on composition was determined using catalysts of 10.3 wt% N pyrolyzed at 700 °C, 800 °C and 900 °C, and an iron-free sample of 10.3 wt% N pyrolyzed at 800 °C was also studied. As detailed in Table 2, all samples consist of 96–98 at% C, 0.6–2.0 at% O, 0.6–2.0 at% N and low-levels of Fe (<0.3 at%). The addition of Fe (in the form of iron-acetate) to the 1.5 wt% N sample increases observed oxygen content three-fold at the expense of a three-fold decrease in nitrogen content. Insignificant changes in composition due to pyrolysis are observed for the 1.5 wt% N sample: Slightly increased O and N are found, but observed Fe content decreases during pyrolysis.

Increasing the pyrolysis temperature (at 10.3 wt% nominal N) results in increased C content and a decrease in both N and Fe content. It can be observed from Fig. 3 that surface nitrogen composition, as determined by XPS, and bulk nitrogen determined by CHN increase with increasing nominal nitrogen content for all samples. Surface and bulk N content increases rapidly beyond 10.3 wt% N, again attributable to deposits of partially decomposed bipyridine at high nominal nitrogen.

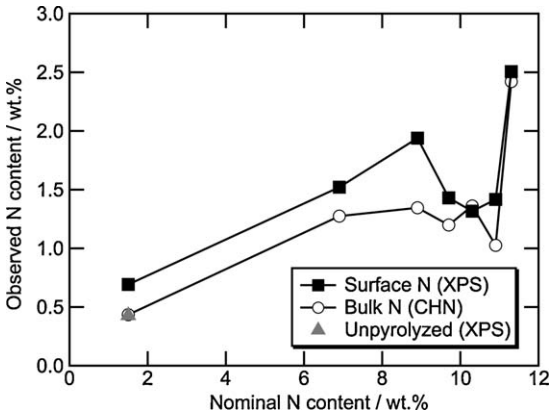

Fig. 3. Surface and bulk nitrogen content obtained through XPS and CHN analyses respectively as a function of nominal nitrogen loading. XPS results have been converted to units of wt% for comparison purposes.

High-resolution N 1s spectra of all samples were fitted using four components: pyridinic (~398.4 eV), amine or iron-associated pyridinic (~399.3 eV), quaternary (~401.0 eV), and graphitic (~403.3 eV) nitrogen species. Fig. 4a and b show nitrogen spectra and curve-fits for as-synthesized catalysts of 1.5 wt% N prior to pyrolysis, without (Fig. 4a) and with (Fig. 4b) added iron from iron-acetate. The pyridinic peak dominates these spectra and little difference is observed except a small increase in the peak at

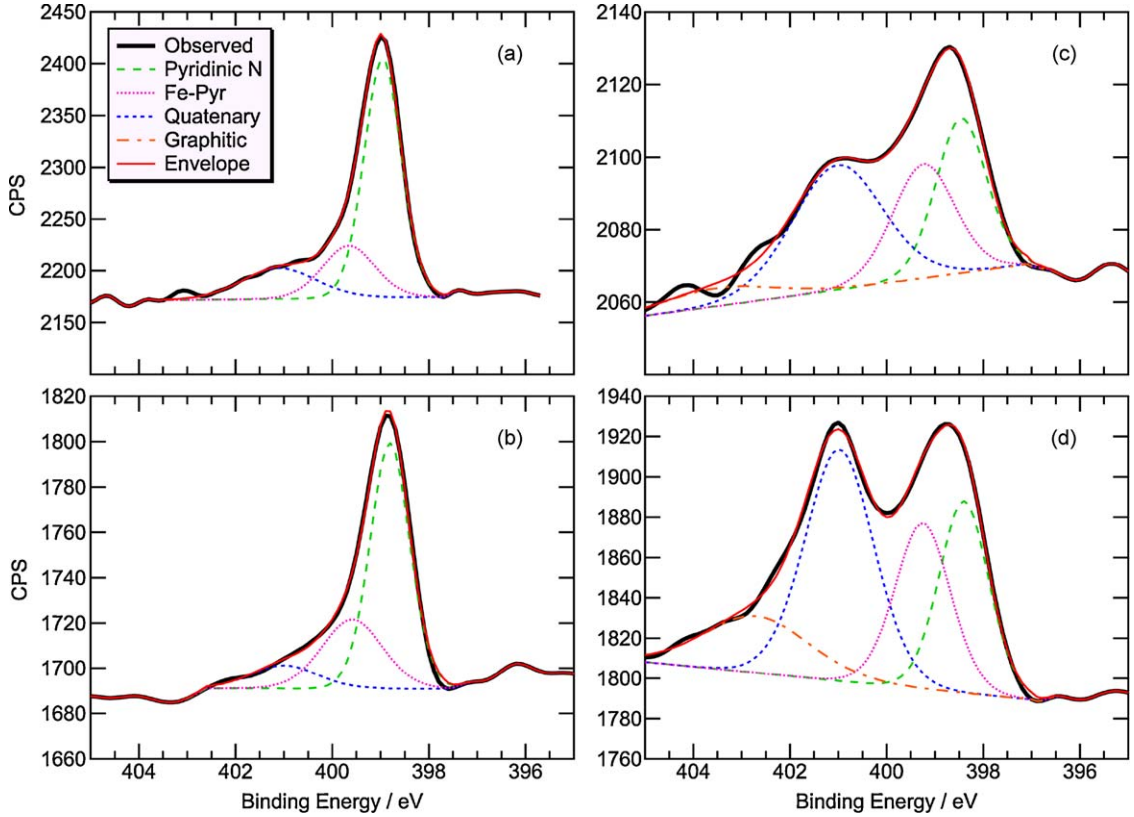

Fig. 4. High-resolution N 1s spectra deconvoluted for a subset of samples (a) As synthesized catalyst (1.5 wt% nominal N, no Fe) before pyrolysis; (b) As-synthesized catalyst (1.5 wt% nominal N) before pyrolysis; (c) Pyrolyzed catalyst (1.5 wt% nominal N); (d) Pyrolyzed catalyst (10.3 wt% nominal N).

Table 3
Deconvolution results (at%) for N 1s high-resolution spectra.

Nominal N (wt%)	Pyrolysis Temp. (°C)	Pyridinic (398.4 eV)	Fe–Pyr (399.3 eV)	Quaternary (401.0 eV)	Graphitic (403.3 eV)
1.5 (no Fe)	–	0.67	0.18[†]	0.12	–
1.5	–	0.22	0.10	0.05	–
1.5	800	0.20	0.14	0.24	0.03
6.9	800	0.36	0.17	0.69	0.09
8.9	800	0.49	0.17	0.94	0.08
9.7	800	0.41	0.14	0.55	0.15
10.3	700	0.41	0.28	0.50	0.07
10.3	800	0.27	0.24	0.50	0.13
10.3	900	0.17	0.05	0.35	0.08
10.9	800	0.34	0.19	0.63	0.07
11.3	800	0.48	0.12	1.23	0.35

[†] In the absence of Fe, this peak may be attributable to amine type N.

399.3 eV that may be attributable to increased iron-associated pyridinic (Fe–Pyr) moieties. As shown in Fig. 4c and d, pyrolysis appears to increase the prominence of the quaternary and graphitic peaks.

Table 3 shows deconvoluted N 1s results for all samples. Unpyrolyzed samples without Fe contain 0.18 at% N at 399.3 eV, attributable to amine nitrogen species. Addition of Fe-acetate decreases this content to 0.10 at%, ascribed to the overall decrease in nitrogen content discussed above. Relative to the other components, this component actually increases upon addition of Fe-acetate, and can thus be interpreted as Fe^{2+} coordinated with pyridinic nitrogen (Fe–Pyr).

Pyrolysis decreases pyridinic N and increases quaternary N content. The lowest levels of pyridinic nitrogen content were observed for the sample pyrolyzed at 900 °C, suggesting that higher pyrolysis temperature leads to increased conversion of pyridinic nitrogen to quaternary and graphitic nitrogen.

Fig. 5 shows the trends for all nitrogen species as a function of nominal nitrogen content. The absolute content of all species increases as nominal N content increases up to 9 wt% N, beyond which Fe–Pyr content shows a maximum and pyridinic and quaternary N decrease to a minimum. This volatility occurs close to the point at which surface area drops precipitously (Fig. 2), suggesting partially decomposed bipyridine mass may cover or screen out some nitrogen species existing on the high surface area support.

Gloaguen et al. proposed the use of RDE measurements as a fast screening tool for the characterization of supported catalysts with respect to their ORR activity [38]. Fig. 6 shows the polarization curves recorded at 1200 rpm and 40 °C for a series of catalysts synthesized at 800 °C with precursor nitrogen content varying from 1.5 to 11.3 wt%. An increase in the onset potential is observed with increasing N content up to 10.3 wt%. Beyond this value,

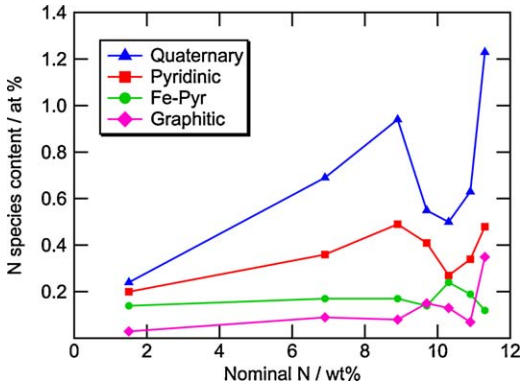

Fig. 5. Surface nitrogen content of pyrolyzed catalysts as determined by XPS for varying nominal nitrogen loading.

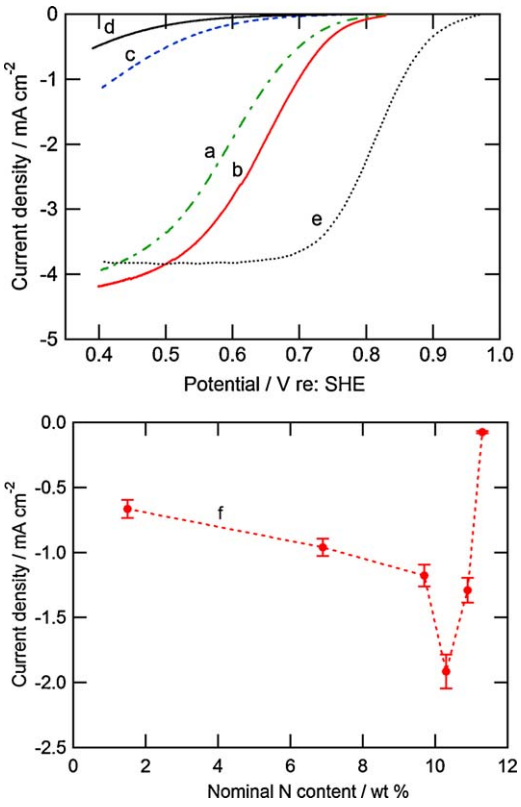

Fig. 6. Oxygen reduction at thin-film rotating disk electrodes with Fe–N–C catalysts of varying composition in O_2-saturated, 1N aqueous sulfuric acid, 40 °C. Pseudo-steady state polarization: Scan rate 0.5 mV s^{-1}, rotation rate 1200 rpm. (a) 6.9 wt% nominal N, (b) 10 .3 wt% (c) 11.3 wt%, (d) 10.3 wt%, w/o Fe, (e) 20 wt% Pt/C [ETEK], (f) Current density at 0.65 V/SHE as a function of nominal nitrogen content.

further increase in nominal N content results in a very high overpotential towards ORR, exemplified by data for 11.3 wt% N. This overpotential is possibly due to excess partially decomposed bipyridine, as discussed above. In the absence of any precursor metal, a very high over-potential is observed, confirming the significance of the metal precursor in the generation of active sites [1,25]. Fig. 6b shows the dependence of catalyst activity on N content at 0.65 V/SHE, where the current is controlled mainly by ORR kinetics and where the 10.3 wt% N catalyst showed the highest current density. Beyond 10.3 wt% N, the activity of the catalysts decreased, again attributable to excess partially decomposed bipyridine that imparts transport limitations in the catalysts due to pore closure. Higher mesoporosity in the carbon-support may ameliorate such effects, and hence a material displaying a combination of microporosity and mesoporosity may be ideal.

Pyrolysis temperature effects on catalyst activity are shown in Fig. 7. Catalysts pyrolyzed at 700 °C and 800 °C shows similar onset potential, however the catalyst pyrolyzed at 800 °C showed improved kinetics. Loss of activity at 900 °C could be due to poor fixation of nitrogen in the carbon-support, as suggested by XPS analysis.

Koutecky-Levich analysis was conducted for the ORR using catalysts of 10.3 wt% nominal nitrogen at potentials in the range of 0.65–0.5 V/SHE. The charge-transfer limited current density at the electrode surface, i_k, was obtained by

$$\frac{1}{i} = \frac{1}{i_k} + \frac{1}{i_{lim}} \quad (1)$$

where i is the current density observed at the RDE and $i_{lim} = B\sqrt{\omega}$ is the mass-transfer limited current density at the RDE, with ω the

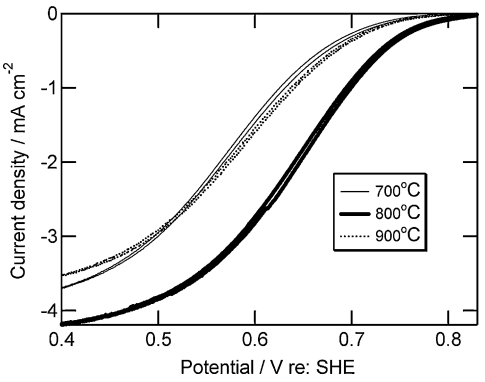

Fig. 7. Polarization curves showing the effect of heat-treatment temperature on the catalytic activity towards ORR. Conditions as in Fig. 6.

electrode rotation rate in radians per second, and B the Levich slope given as [39]

$$B = 0.62nFC_{O_2}D^{2/3}\nu^{-1/6} \quad (2)$$

where n is the electron stoichiometry for the ORR, F the Faraday constant, D the diffusion coefficient for oxygen in 1N H_2SO_4 solution (1.93×10^{-5} cm^2 s^{-1}) [40], C_{O2} the concentration of dissolved oxygen (1.26×10^{-6} mol cm^{-3}) [41], and ν the kinematic viscosity of sulfuric acid (0.01 cm^2 s^{-1})[42]. Plots of i^{-1} versus $\omega^{-1/2}$ are shown in Fig. 8a for potentials of 0.65–0.5 V/SHE. Linearity in the fit can be observed at all potentials with less than 2% standard deviation. The nearly parallel slopes observed in Fig. 8a confirms that the ORR follows first-order kinetics and electron stoichiometry does not vary substantially in this potential range [39]. From the slope, the electron stoichiometry was estimated to be

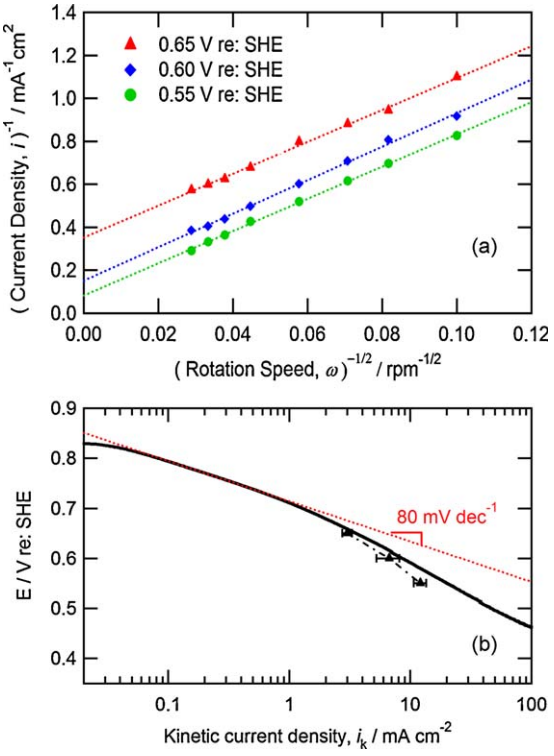

Fig. 8. Koutecky-Levich analysis performed on the catalyst having a nominal N content of 10.3 wt% at 40 °C in 1N aqueous sulfuric acid. (a) Koutecky-Levich plot obtained at three potentials. (b) Tafel plot for the corresponding catalyst, conditions as in Fig. 6.

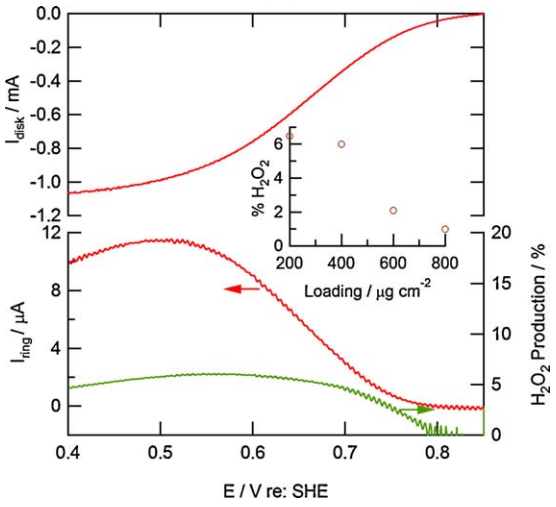

Fig. 9. Peroxide generation during ORR at Fe-N-C catalysts via rotating ring-disk (RRDE) experiments. Polarization of disk (top) and ring (bottom left) obtained through RRDE measurements of the catalyst having a nominal N content of 10.3 wt%. The percentage H_2O_2 produced is plotted bottom right. Inset: Percentage H_2O_2 generated for varying catalyst loading. All conditions as in Fig. 6.

$n = 3.57 \pm 0.07$, indicating a nearly complete reduction of oxygen to water. Fig. 8b shows mass-transfer-corrected Tafel plots for the same catalyst. The mass-transfer correction was done using the relation,

$$i_k = \frac{i_{lim}\, i}{(i_{lim} - i)} \quad (3)$$

using i_{lim} obtained from Fig. 6. The calculated Tafel slope at potentials lower than 0.7 V/SHE is 130 mV dec^{-1}, close to theoretical value of 120 mV dec^{-1} for a one electron rate-determining step. The Tafel slope obtained above 0.7 V/SHE is 80 mV dec^{-1} and a corresponding exchange current density of 4×10^{-7} mA cm^{-2} was observed at the reversible potential of 0.93 V/SHE.

Rotating ring disc electrode (RRDE) studies was performed to quantify hydrogen peroxide production and selectivity of the ORR toward water production. The disc potential was scanned at 0.5 mV s^{-1}, while the ring electrode was held at 1.2 V/SHE, a potential sufficiently high to oxidize any peroxide formed during the ORR. Fig. 9 shows the disk and ring currents obtained using the optimal catalyst (10.3 wt% N). The electron stoichiometry, n, and fractional H_2O_2 formation, $\chi_{H_2O_2}$ were determined from the collection efficiency ($N = 0.39$), ring current, I_{ring}, and disk current, I_{disk}, by [43]

$$n = \frac{4I_{disk}}{I_{disk} + I_{ring}/N} \quad (4)$$

$$\chi_{H_2O_2} = \frac{2I_{ring}/N}{I_{disk} + I_{ring}/N} \quad (5)$$

Poor stability of similar metal-nitrogen-carbon catalysts has been attributed to the attack of active sites by H_2O_2 generated during oxygen reduction [44–46]. As shown in Fig. 9, the fractional peroxide generation remained near 6% in the range 0.4–0.9 V/SHE, and the electron stoichiometric number remained near 3.88 [plot not shown], demonstrating high selectivity toward 4 e$^-$ reduction of oxygen to water. It has been demonstrated that the amount of H_2O_2 generated depends strongly on catalyst loading on the RRDE, associated with residence time of the peroxide intermediate within the porous catalyst [47]. The inset in Fig. 9 shows the effect

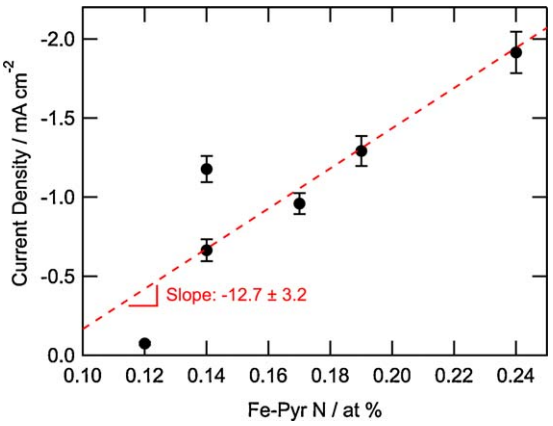

Fig. 10. Correlation of Fe–Pyr nitrogen content to current density at 0.65 V/SHE.

of catalyst loading on peroxide generation at 0.6 V/SHE. The observed maximum in $\chi_{H_2O_2}$ is about 6.5% at 200 μg cm^{-2}, lower than values reported for similar catalysts [47]. However, under real fuel cell conditions, the thickness of the cathode catalyst layer is about 100 μm, corresponding to a loading of ca. 2–3 mg cm^{-2}. Hence the amount of hydrogen peroxide generated would be less significant due to the higher residence time and therefore more complete reduction.

The correlation between ORR current density at 0.65 V/SHE and Fe–Pyr content obtained by XPS is shown in Fig. 10. Samples containing 10.3 wt% nominal N, for which the largest current density is observed, also displayed the largest Fe–Pyr content (0.24 wt%). The overall trend indicates that increased Fe–Pyr content leads to increased catalyst activity. Current density correlated poorly with variations in the content of other nitrogen species (not shown). These results suggest that the pyridinic form of nitrogen coordinated with Fe is associated with the active site of the catalyst.

Compared to previous reports of metal-nitrogen-carbon ORR catalysts using Ketjenblack® as the carbon-support, we demonstrate more than two-fold increase in the nitrogen surface content [12]. The optimized catalyst also exhibits an open-circuit potential of 0.83 V/NHE, 0.1 V higher than previous results [48]. In RDE-based experiments, the present observed current density is about 3.5-fold higher at 0.55 V/SHE and at least 15-fold higher at 0.7 V/SHE and 27 °C (data not shown). Charreteur et al. compare the ORR activity of their catalysts based on V_{pr}, the potential of peak ORR current in a cyclic voltammetric scan, which is directly proportional to the logarithm of exchange current density [24]. V_{pr} measured with our optimized catalysts is 0.73 V/SHE, equivalent to the highest value reported by Charreteur et al. for catalysts supported on developmental carbon. Although surface N content in the optimal catalyst is about 1.5%, smaller than the value reported by Charreteur et al., the catalytic activity is comparable.

4. Conclusions

Active Fe–N based electrocatalysts have been prepared using Ketjenblack® as a carbon-support and bipyridine as a nitrogen-bearing precursor, by pyrolysis in a quartz ampule at high pressure. Improved catalytic activity is obtained by tuning the amount of precursor nitrogen, introduced in the form of bipyridine. In comparison to the use of flowing nitrogen gas at atmospheric pressure, this approach allows amplification and control of nitrogen activity during pyrolysis. A two-fold increase in surface nitrogen content is obtained which correlates with increased open-circuit potential and improved ORR kinetics in the potential region of interest for operating fuel cells. The current density obtained at 0.65 V/SHE increases with increasing Fe-pyridinic nitrogen content, indicating the significance of this species as part of the catalytic site. An optimized catalyst obtained in this work demonstrates nearly complete reduction of oxygen into water with high selectivity in the potential range of interest. A key path to improve on these results may be the use of carbon-support having a combination of microporosity and mesoporosity that simultaneously maximizes active site density and oxygen transport. Moreover, the stability of the present catalysts in acid media is an ongoing concern that is best addressed by studies of membrane electrode assemblies prepared with these catalysts.

References

[1] F. Jaouen, J.P. Dodelet, Electrochim. Acta 52 (2007) 5975–5984.
[2] A.K. Shukla, R.K. Raman, Annu. Rev. Mater. Res. 33 (2003) 155–168.
[3] Y.K. Sun, J. Appl. Electrochem. 31 (2001) 1149–1153.
[4] G.Q. Sun, J.T. Wang, R.F. Savinell, J. Appl. Electrochem. 28 (1998) 1087–1093.
[5] C.W.B. Bezerra, L. Zhang, K.C. Lee, H.S. Liu, A.L.B. Marques, E.P. Marques, H.J. Wang, J.J. Zhang, Electrochim. Acta 53 (2008) 4937–4951.
[6] R. Jasinski, Nature 201 (1964) 1212–1213.
[7] K. Wiesener, D. Ohms, V. Neumann, R. Franke, Mater. Chem. Phys. 22 (1989) 457–475.
[8] S. Gupta, D. Tryk, I. Bae, W. Aldred, E. Yeager, J. Appl. Electrochem. 19 (1989) 19–27.
[9] S.L. Gojkovic, S. Gupta, R.F. Savinell, J. Electrochem. Soc. 145 (1998) 3493–3499.
[10] P. Gouerec, A. Biloul, O. Contamin, G. Scarbeck, M. Savy, J. Riga, L.T. Weng, P. Bertrand, J. Electroanal. Chem. 422 (1997) 61–75.
[11] K. Sawai, N. Suzuki, J. Electrochem. Soc. 151 (2004) A682–A688.
[12] F. Jaouen, S. Marcotte, J.P. Dodelet, G. Lindbergh, J. Phys. Chem. B 107 (2003) 1376–1386.
[13] M. Bron, J. Radnik, M. Fieber-Erdmann, P. Bogdanoff, S. Fiechter, J. Electroanal. Chem. 535 (2002) 113–119.
[14] C.Z. Deng, M.J. Dignam, J. Electrochem. Soc. 145 (1998) 3507–3512.
[15] R. Bashyam, P. Zelenay, Nature 443 (2006) 63–66.
[16] M. Lefevre, J.P. Dodelet, P. Bertrand, J. Phys. Chem. B 106 (2002) 8705–8713.
[17] M. Lefevre, J.P. Dodelet, P. Bertrand, J. Phys. Chem. B 109 (2005) 16718–16724.
[18] E. Proietti, S. Ruggeri, J.P. Dodelet, J. Electrochem. Soc. 155 (2008) B340–B348.
[19] P.H. Matter, E. Wang, U.S. Ozkan, J. Catal. 243 (2006) 395–403.
[20] P.H. Matter, L. Zhang, U.S. Ozkan, J. Catal. 239 (2006) 83–96.
[21] S. Maldonado, K.J. Stevenson, J. Phys. Chem. B 109 (2005) 4707–4716.
[22] V. Nallathambi, J.W. Lee, S.P. Kumaraguru, G. Wu, B.N. Popov, J. Power Sources 183 (2008) 34–42.
[23] S. Ruggeri, J.P. Dodelet, J. Electrochem. Soc. 154 (2007) B761–B769.
[24] F. Charreteur, F. Jaouen, S. Ruggeri, J.P. Dodelet, Electrochim. Acta 53 (2008) 2925–2938.
[25] J.M. Ziegelbauer, T.S. Olson, S. Pylypenko, F. Alamgir, C. Jaye, P. Atanassov, S. Mukerjee, J. Phys. Chem. C 112 (2008) 8839–8849.
[26] T.E. Wood, Z. Tan, A.K. Schmoeckel, D. O'Neill, R. Atanasoski, J. Power Sources 178 (2008) 510–516.
[27] G. Wei, J.S. Wainright, R.F. Savinell, J. New Mater. Electrochem. Syst. 3 (2000) 121–129.
[28] M. Lefevre, J.P. Dodelet, P. Bertrand, J. Phys. Chem. B 104 (2000) 11238–11247.
[29] H. Schulenburg, S. Stankov, V. Schunemann, J. Radnik, I. Dorbandt, S. Fiechter, P. Bogdanoff, H. Tributsch, J. Phys. Chem. B 107 (2003) 9034–9041.
[30] J.R. Pels, F. Kapteijn, J.A. Moulijn, Q. Zhu, K.M. Thomas, Carbon 33 (1995) 1641–1653.
[31] D. Villers, X. Jacques-Bedard, J.P. Dodelet, J. Electrochem. Soc. 151 (2004) A1507–A1515.
[32] K. Stanczyk, R. Dziembaj, Z. Piwowarska, S. Witkowski, Carbon 33 (1995) 1383–1392.
[33] A.N. Buckley, Fuel Process. Technol. 38 (1994) 165–179.
[34] E.P. Barrett, L.G. Joyner, P.P. Halenda, J. Am. Chem. Soc. 73 (1951) 373–380.
[35] U.A. Paulus, T.J. Schmidt, H.A. Gasteiger, R.J. Behm, J. Electroanal. Chem. 495 (2001) 134–145.
[36] S. Pylypenko, S. Mukherjee, T. Olson, P. Atanassov, Electrochim. Acta 53 (2008) 7875–7883.
[37] G.Q. Sun, J.T. Wang, S. Gupta, R.F. Savinell, J. Appl. Electrochem. 31 (2001) 1025–1031.
[38] F. Gloaguen, F. Andolfatto, R. Durand, P. Ozil, J. Appl. Electrochem. 24 (1994) 863–869.
[39] V. Stamenkovic, T.J. Schmidt, P.N. Ross, N.M. Markovic, J. Phys. Chem. B 106 (2002) 11970–11979.
[40] N.A. Anastasijevic, Z.M. Dimitrijevic, R.R. Adzic, Electrochim. Acta 31 (1986) 1125–1130.
[41] A. Schumpe, I. Adler, W.D. Deckwer, Biotechnol. Bioeng. 20 (1978) 145–150.
[42] M. Pattabi, R.H. Castellanos, R. Castillo, A.L. Ocampo, J. Moreira, P.J. Sebastian, J.C. McClure, X. Mathew, Int. J. Hydrogen Energy 26 (2001) 171–174.
[43] T.J. Schmidt, U.A. Paulus, H.A. Gasteiger, N. Alonso-Vante, R.J. Behm, J. Electrochem. Soc. 147 (2000) 2620–2624.

[44] B. Wang, J. Power Sources 152 (2005) 1–15.
[45] H.S. Liu, C.J. Song, Y.H. Tang, J.L. Zhang, H.J. Zhang, Electrochim. Acta 52 (2007) 4532–4538.
[46] C. Fierro, A.B. Anderson, D.A. Scherson, J. Phys. Chem. 92 (1988) 6902–6907.
[47] A. Bonakdarpour, M. Lefevre, R.Z. Yang, F. Jaouen, T. Dahn, J.P. Dodelet, J.R. Dahn, Electrochem. Solid-State Lett. 11 (2008) B105–B108.
[48] S. Marcotte, D. Villers, N. Guillet, L. Roue, J.P. Dodelet, Electrochim. Acta 50 (2004) 179–188.